materials

MDPI

Article

Enhanced Cycleability of Amorphous MnO_2 by Covering on α-MnO_2 Needles in an Electrochemical Capacitor

Quanbing Liu [1], Shan Ji [2,*], Juan Yang [3], Hui Wang [3], Bruno G. Pollet [4] and Rongfang Wang [3,*]

1 School of Chemical Engineering and Light Industry, Guangdong University of Technology, Guangzhou 510006, China; liuqb@gdut.edu.cn
2 College of Biological, Chemical Science and Chemical Engineering, Jiaxing University, Jiaxing 314001, China
3 Institute of Chemical Engineering, Qingdao University of Science and Technology, Qingdao 266042, China; jing.kuang@firebright1.com (J.Y.); wanghui3931@126.com (H.W.)
4 Renewable Energy Group, Department of Energy and Process Engineering, Faculty of Engineering, Norwegian University of Science and Technology (NTNU), 7491 Trondheim, Norway; bruno.g.pollet@ntnu.no
* Correspondence: jissshan@126.com (S.J.); wrf38745779@126.com (R.W.); Tel.: +86-573-82315109 (S.J.); +86-931-7971533 (R.W.)

Received: 13 July 2017; Accepted: 10 August 2017; Published: 24 August 2017

Abstract: An allomorph MnO_2@MnO_2 core-shell nanostructure was developed via a two-step aqueous reaction method. The data analysis of Scanning Electron Microscopy, Transmission Electron Microscopy, X-Ray Diffraction and N_2 adsorption-desorption isotherms experiments indicated that this unique architecture consisted of a porous layer of amorphous-MnO_2 nano-sheets which were well grown onto the surface of α-MnO_2 nano-needles. Cyclic voltammetry experiments revealed that the double-layer charging and Faradaic *pseudo*-capacity of the MnO_2@MnO_2 capacitor electrode contributed to a specific capacitance of 150.3 $F \cdot g^{-1}$ at a current density of 0.1 $A \cdot g^{-1}$. Long cycle life experiments on the as-prepared MnO_2@MnO_2 sample showed nearly a 99.3% retention after 5000 cycles at a current density of 2 $A \cdot g^{-1}$. This retention value was found to be significantly higher than those reported for amorphous MnO_2-based capacitor electrodes. It was also found that the remarkable cycleability of the MnO_2@MnO_2 was due to the supporting role of α-MnO_2 nano-needle core and the outer amorphous MnO_2 layer.

Keywords: manganese dioxide; core-shell structure; porous; electrochemical capacitors; long stability

1. Introduction

Electrochemical Capacitors (ECs) have been considered as promising electrochemical Energy Storage Devices (ESDs) due to their inherent advantages, such as high power density, long cycle life, high safety factor and environmentally benign nature [1]. With features complementary to batteries and fuel cells, ECs have been widely used as ESDs in many areas, such as in Smart Grids, Electric Vehicles (EVs) and Fuel Cell power systems [2]. Various transition metal oxides have been studied for ECs because of high capacitance originated of solid-state peseudofaradaic reaction, abundance and environmentally friendly properties. Among them, manganese dioxide (MnO_2), a widely used cathode material in battery technologies, has been an attractive material in the area of ECs because of its advantageous properties [3–7]. In comparison to the multiple crystallographic MnO_2 forms, amorphous MnO_2 has been considered a predominant candidate as an EC electrode material due to its large initial capacity [8–10]. However, due to the poor cycleability of amorphous MnO_2, this material has not been extensively used in ECs [11].

On the other hand, core-shell nanostructured MnO_2@MnO_2 can significantly improve the long cycling stability of MnO_2, i.e., 90% retention after 20,000 cycles at a current density of 5 $A \cdot g^{-1}$. The authors found that the superior cycleability of the MnO_2@MnO_2 material was due to the core-shell nanostructure in which the wire-like ß-MnO_2 core provided a stable structural backbone [12]. Similar findings were recently reported by Ma and co-workers who showed that the α-MnO_2 nanowires acted as the stable backbone for δ-MnO_2 nano-sheets to form a hierarchical structured composite which exhibited excellent cycling stability values, e.g., 98.1% retention after 10,000 charge-discharge cycles [13]. Furthermore, the cycling stabilities of both core-shell nanostructured MnO_2@MnO_2 electrodes are distinctly superior to those reported for other core-shell nanostructures composed of other transition metal oxides and MnO_2 such as Co_3O_4@MnO_2 [14–16], SnO_2@MnO_2 [17], NiO-MnO_2 [18], and $NiCo_2O_4$/MnO_2 [19].

Inspired and excited by the above findings in the literature, we produced a hierarchically allomorph α-MnO_2@amorphous MnO_2 core-shell structure, in which α-MnO_2 needles were the core and amorphous MnO_2 nano-sheets the shell. It was found that when the core-shell MnO_2@MnO_2 composite was used as an electrode, well-dispersed amorphous MnO_2 layers on α-MnO_2 needles allowed a fast, reversible Faradic reaction and enabled ion diffusion (due to the porous nature of the material). It was observed that a one-dimensional α-MnO_2 needles acted as the backbone which maintained the structural integrity during the charge-discharge process, thus enhancing the cycling life of the shell. In addition, its porous feature of amorphous MnO_2 (248.9 $m^2 \cdot g^{-1}$) also provided more contact area with the electrolyte, consequently the active surface was greatly improved. As expected, our designed α-MnO_2@amorphous MnO_2 hierarchical electrode exhibited a long-term stability during the cycling tests together with high specific capacitance and rate capability values.

2. Experimental

2.1. Synthesis of α-MnO_2@amorphous MnO_2

All chemical reagents were of high purity AR grade and used as received. The hierarchically core−shell α-MnO_2@amorphous MnO_2 nanostructure material was synthesized in two steps. In the first step, α-MnO_2 needles were prepared by a hydrothermal reaction. Twenty milliliters of 8 $mmol \cdot L^{-1}$ $KMnO_4$ solution was added into 20 mL of 4 $mmol \cdot L^{-1}$ $MnSO_4$ solution with vigorous stirring. The above solution was topped up to 80 mL with ultra-pure water and then transferred to a 100 mL Teflon-lined autoclave, and heated at 140 °C for 12 h. Thereafter, the autoclave was allowed to cool to ambient temperature. The resulting solid product was collected by centrifugation, washed thoroughly with distilled water and then dried overnight in air at 60 °C. In the second step, the as-synthesized α-MnO_2 needles were dispersed in 30 mL of 0.41 $mmol \cdot L^{-1}$ $MnSO_4$ solution with vigorous stirring. Subsequently, 20 mL of 0.28 $mmol \cdot L^{-1}$ $KMnO_4$ solution was added dropwise to the above solution. The reaction was maintained for 12 h. After that, the resulting solid product denoted as "MnO_2@MnO_2" was collected by centrifugation, washed thoroughly with distilled water and then dried overnight in air at 60 °C. For comparison purposes, amorphous MnO_2 nano-sheets were also prepared in which the second-step procedure and materials were used but without the addition of the α-MnO_2 needles.

2.2. Characterizations

X-ray diffraction (XRD) was carried out using a Shimadzu XD-3A (Shimadzu, Kyoto, Japan) fitted with a filtered Cu-Kα radiation (λ = 0.15418 nm) generated at 40 kV and 30 mA. The sorption isotherms were obtained on a Quantachrome Autosorb-1 volumetric analyzer. Specific surface area was determined by the Brunauer-Emmett-Teller (BET) method and the Density Functional Theory (DFT) was used for analyzing the full range of pore size distribution. Scanning Electron Microscopy (SEM) images were obtained on Carl Zeiss Ultra Plus (Carl Zeiss Microscopy GmbH, Jena, Germany). Fine structures were analyzed by Transmission Electron Microscopy (TEM) using a JEM-2010 (JEOL Ltd, Tokyo, Japan) microscope.

2.3. Electrochemical Measurements

Cyclic voltammograms (CV) and galvanostatic charge/discharge experiments were performed to evaluate the electrochemical behaviour of α-MnO_2@amorphous MnO_2 in a three-electrode cell configuration. The working electrode (WE) was fabricated by pasting a homogeneous slurry of α-MnO_2@amorphous MnO_2, carbon black and poly(tetrafluoroethylene) with a mass ratio of 80:10:10 into ethylene glycol, and then the mixture was rolled out to form uniform slices, followed by drying at 80 °C for 6 h. Subsequently, the slices were pressed onto a stainless steel (1 cm × 1 cm) plate with a tablet press. The amount of electrode material on the electrode was approximately 10 mg.

A three-electrode cell was used for the electrochemical experiments, in which the reference electrode (RE) was an Hg/HgO (1 M KOH) electrode and active carbon is working electrode (WE). The electrolyte was a 1.0 mol·L^{-1} LiOH. CV experiments were performed in the potential range (−0.14 V vs. Hg/HgO and +0.61 V vs. Hg/HgO) (0 to 0.75 V vs. SHE (standard hydrogen electrode)) at different scan rates of 2, 5, 10, 20 and 50 mV·s^{-1} on a CHI 650D electrochemical workstation. Galvanostatic charge/discharge (from −0.14 to 0.61 V vs. Hg/HgO) and cycle life tests were carried out using a Neware Battery Tester (Shengzhen Neware Technology Company, Shengzhen, China). Electrochemical Impedance Spectroscopy (EIS) analyses (Metrohm, Utrecht, The Netherlands) were performed between 10 kHz and 0.01 Hz using a 5 mV *RMS* sinusoidal modulation at the Open Circuit Potential (OCP).

3. Results and Discussion

In this study, α-MnO_2 was synthesized in the first step by a hydrothermal process via the following reaction:

$$2KMnO_4 + 3MnSO_4 + 2H_2O \rightarrow 5MnO_2 + K_2SO_4 + 2H_2SO_4 \quad (1)$$

The XRD pattern of the material, shown as the black line in Figure 1, displays diffraction peaks characteristics for tetragonal α-MnO_2 (JCPDS PDF 72-1982) [20]. The products obtained at the second step shown as the red line exhibit two broad diffraction peaks at around 37° and 66°, indicating the amorphous nature of the MnO_2 sample [9]. When the amorphous MnO_2 grew on the α-MnO_2, the XRD pattern of MnO_2@MnO_2 (shown as the blue line) displays the characteristics of the two MnO_2 samples, suggesting that the presence of the α-MnO_2 base did not affect the structure of the amorphous MnO_2.

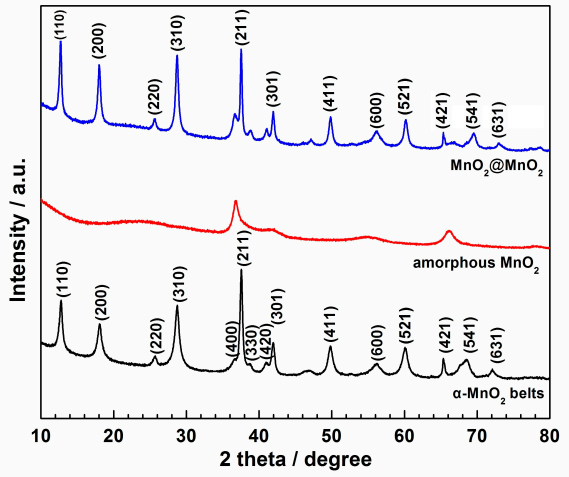

Figure 1. XRD patterns of MnO_2@MnO_2, α-MnO_2 and amorphous MnO_2 samples.

Figure 2 shows the morphologies of the three samples. It can be observed in Figure 2a that the as-prepared α-MnO_2 needles have a width of 50–150 nm and a length extending from 1 to 5 μm. The inset of Figure 2a indicates that the needle-like α-MnO_2 surface is smooth. The SEM image of

MnO_2@MnO_2 shown in Figure 2b reveals that the length of the needles was kept unchanged. The high resolution SEM image in Figure 2c clearly shows a cotton-like surface, resulting from the uniform growth of amorphous MnO_2. Meanwhile, no packed amorphous MnO_2 was observed in the space among the needles, indicating that the amorphous MnO_2 preferred to cover on the surface of the α-MnO_2 needles. When the α-MnO_2 needles were not present, the amorphous MnO_2 would aggregate into pompom-like clusters.

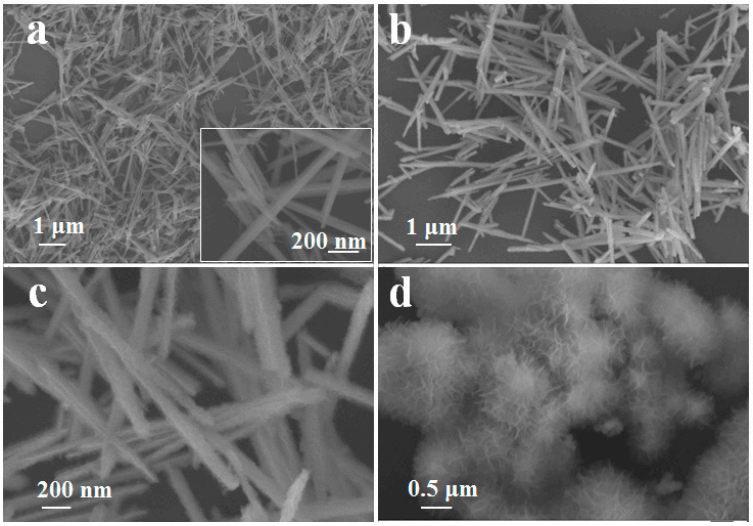

Figure 2. SEM images of: (**a**) α-MnO_2 needles; (**b**,**c**) MnO_2@MnO_2; and (**d**) amorphous MnO_2.

Further structural characterizations of the MnO_2@MnO_2 were carried out by TEM. Figure 3a shows a typical TEM image of the MnO_2@MnO_2, revealing that the hierarchically nanostructure is constructed by numerous thin nano-sheet "shells" covered on the needle "core", which is in very good agreement with the SEM observation. From Figure 3b, it was possible to determine a shell thickness of ca. 50 nm. The figure also shows that the shell layer had an open structure with the interconnected nano-sheets creating abundant space. High resolution TEM of the shell in Figure 3c did not display clear lattice fringe, indicating poor crystallinity of the shell, which is in agreement with the XRD results. The EDX pattern, shown in Figure 3d, indicates that MnO_2@MnO_2 consisted principally of the elements of manganese and oxygen.

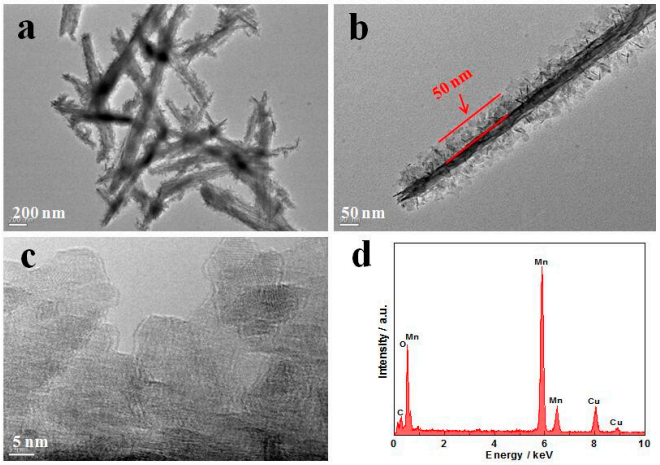

Figure 3. (**a**–**c**) TEM images with different magnification; and (**d**) EDX (Energy-dispersive X-ray) spectrum of MnO_2@MnO_2.

N_2 adsorption-desorption isotherms of α-MnO_2, MnO_2@MnO_2 and amorphous MnO_2 are shown in Figure 4. From the figure, it can be observed that α-MnO_2 needles displayed *type II* isotherms according to the IUPAC classification. The isotherms of amorphous MnO_2 could be classified as *type IV* [21]. A distinct hysteresis loop can also be observed in the larger range of 0.4–1.0 P/P_0 indicating a relatively large pore size [22]. When composite α-MnO_2 needles and amorphous MnO_2 were both present, *type III* isotherms were observed for MnO_2@MnO_2, which could be the mix of *type II* and *IV* isotherms. Their pore size distributions are shown in Figure 4b. As observed, the three samples had micro- and mesopores; and the amount of the pores increased following the sequence of α-MnO_2 < MnO_2@MnO_2 < amorphous MnO_2. The BET specific surface areas of α-MnO_2, MnO_2@MnO_2 and amorphous MnO_2 were found to be 21.2, 54.4 and 248.9 $m^2 \cdot g^{-1}$, respectively. The total pore volume values calculated from the total nitrogen adsorption were 0.15, 0.28 and 0.41 $cm^3 \cdot g^{-1}$, respectively. The relatively low BET surface area and total pore volume of MnO_2@MnO_2 compared to amorphous MnO_2 can be attributed to the presence of α-MnO_2 in the hierarchical structure.

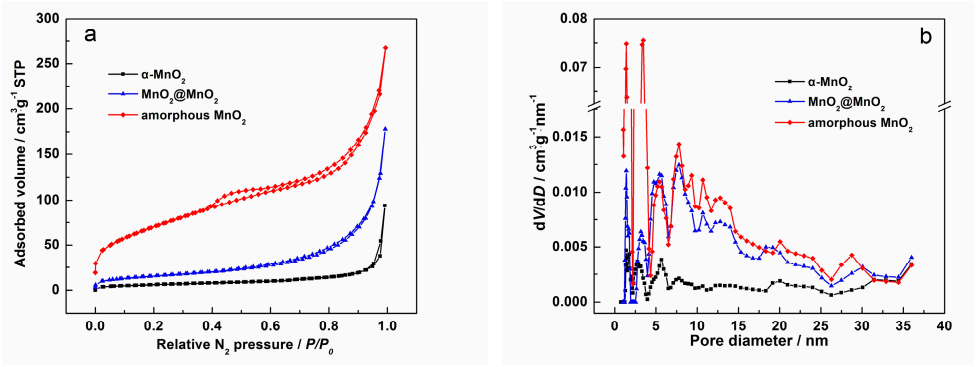

Figure 4. N_2 adsorption-desorption isotherms (**a**) and the pore size distribution (**b**) of α-MnO_2, MnO_2@MnO_2 and amorphous MnO_2.

Electrochemical performance of MnO_2@MnO_2 was firstly studied by Cyclic Voltammetry (CV) in the potential window of (−0.14; +0.61 V (vs. Hg/HgO)). Figure 5 shows cyclic voltammograms recorded at a scan rate of 5 $mV \cdot s^{-1}$. The figure also shows that all CV curves are "roughly" of symmetric rectangular shapes, typical of *pseudo*-capacitive behavior, and the redox peak potentials of +0.49 V and +0.44 V vs. Hg/HgO correspond to the reversible Faradaic redox reaction, indicating that the electrode was charged and discharged through the intercalation/deintercalation of Li^+ into the MnO_2 structure accompanied by the valence conversion of Mn^{4+} to Mn^{3+} [23]. This finding also indicates that the capacitance of the three capacitor electrodes consists of the double-layer charging and Faradaic *pseudo*-capacity. It was found that the voltammetric current response decreased in the following sequence: amorphous MnO_2 > MnO_2@MnO_2 > α-MnO_2, indicating that the capacitance decreased in a similar trend, which could be attributed to a decrease of the BET surface area, leading to a decrease of the double-layer charging.

To further investigate the cyclability of MnO_2@MnO_2, galvanostatic charge/discharge experiments were performed at constant current densities of 0.1 $A \cdot g^{-1}$ as shown in Figure 6. The figure shows that the three samples exhibited linear variation in potential during the charging/discharging process and had *quasi*-symmetrical shapes, indicating a clear contribution from the *pseudo*-capacitive and double layer processes [24]. Based upon the galvanostatic discharge curves, the specific capacitance was calculated according to the following Equation (2):

$$C = I\Delta t / m\Delta V \quad (2)$$

where C ($F \cdot g^{-1}$) is the specific capacitance, I (mA) is the charge-discharge current, Δt (s) is the discharge time, m (mg) represents the mass of the electrode (active material), and ΔV (V) is the potential drop

during discharge. The specific capacitance of the α-MnO_2, MnO_2@MnO_2 and amorphous MnO_2 electrodes were calculated to be 91.2, 150.3 and 247.0 $F \cdot g^{-1}$ respectively. From the data, it can be observed that amorphous MnO_2 exhibited the highest specific capacitances, which resulted from the largest surface area among the three samples. This observation is in excellent agreement with other reported findings which state that the use of amorphous MnO_2 as EC electrode material exhibits large initial capacity compared to the multiple crystallographic MnO_2 forms, as shown in Table 1 [8–10]. It was also found that the specific capacitances of the as-prepared MnO_2@MnO_2 were larger than isomorphous MnO_2@MnO_2 electrode (108 $F \cdot g^{-1}$ at 5 $A \cdot g^{-1}$) [12], but smaller than the allomorph MnO_2@MnO_2 electrode (310.2 $F \cdot g^{-1}$ at 0.5 $A \cdot g^{-1}$) [13]. In addition, it was also observed that the presence of α-MnO_2 is not favorable for the initial capacity of amorphous MnO_2.

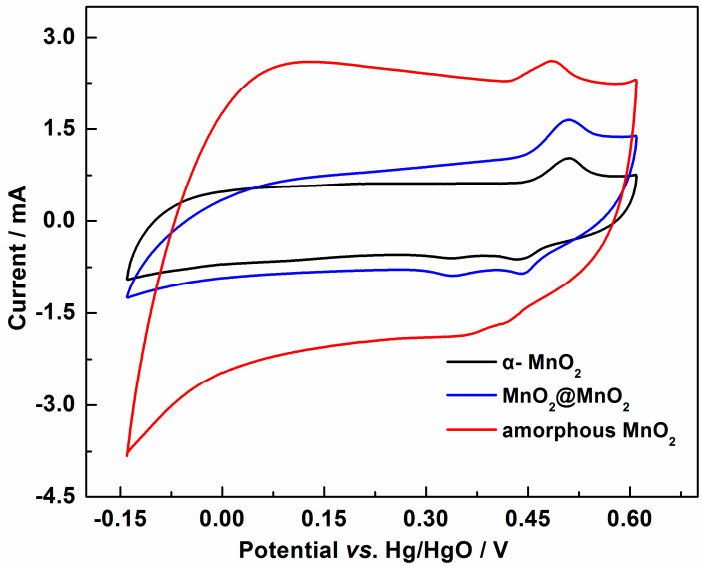

Figure 5. CV curves of the α-MnO_2, MnO_2@MnO_2 and amorphous MnO_2 electrodes at scan rate of 5 $mV \cdot s^{-1}$.

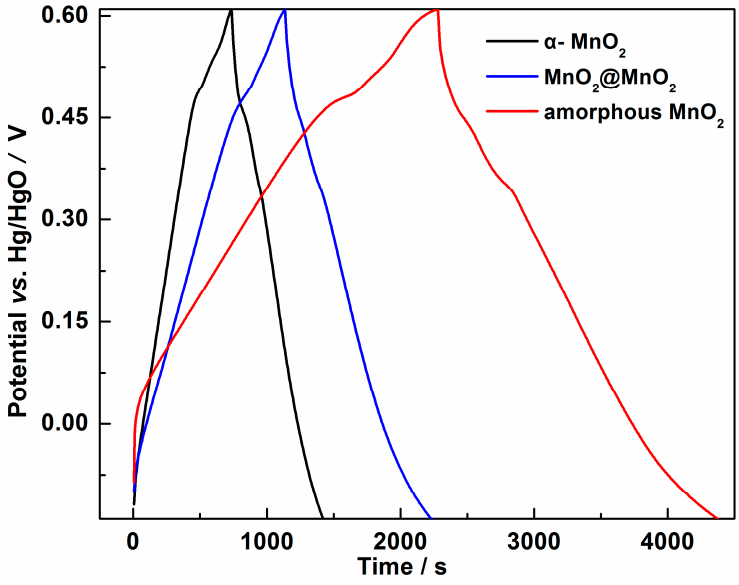

Figure 6. Charge-discharge behavior of the α-MnO_2, MnO_2@MnO_2 and amorphous MnO_2 electrodes at current density of 0.1 $A \cdot g^{-1}$.

Table 1. Comparison of the specific capacitance of as-prepared electrodes to other reported amorphous MnO_2 and MnO_2@MnO_2 electrodes.

Samples	[Ref.]	The specific Capacitance ($F \cdot g^{-1}$)	Electrolyte Type & Concentration	Scan Rate or Current Density
Amorphous MnO_2	herein	247	1.0 M LiOH	0.1 $A \cdot g^{-1}$
MnO_2@MnO_2	herein	150	1.0 M LiOH	0.1 $A \cdot g^{-1}$
Amorphous MnO_2	[8]	242	0.5 M Na_2SO_4	2 $mA \cdot cm^{-2}$
Amorphous MnO_2	[9]	110	2 M NaCl	5 $mV \cdot s^{-1}$
		225	1.0 M Li_2SO_4	
Amorphous MnO_2	[10]	242	1.0 M Na_2SO_4	2 $mV \cdot s^{-1}$
		194	0.5 M K_2SO_4	
Amorphous MnO_2	[25]	79	1.0 M Na_2SO_4	1 $A \cdot g^{-1}$
MnO_2@MnO_2	[12]	108	0.5 M Na_2SO_4	5 $A \cdot g^{-1}$
MnO_2@MnO_2	[13]	310	6.0 M KOH	0.5 $A \cdot g^{-1}$

To evaluate the cyclic stability of the MnO_2@MnO_2 electrode, galvanostatic charge/discharge tests were performed at a current density of 2 $A \cdot g^{-1}$. As shown in Figure 7, after 5000 cycles, the specific capacitance retention of the α-MnO_2, MnO_2@MnO_2 and amorphous MnO_2 electrode remained 99.1%, 99.3% and 77.4% of their initial capacity respectively, indicating a good cyclic stability for α-MnO_2 and MnO_2@MnO_2. As seen in the inset, the comparison of the charge-discharge curves of MnO_2@MnO_2 between the first (1st) and the eighth (8th) cycles indicates that the curves are very stable, further emphasizing the long-term stability of MnO_2@MnO_2. In addition, it was found that the retention of MnO_2@MnO_2 after 5000 cycles was higher than that of many MnO_2-based composite electrodes [14,26–29]. This finding clearly demonstrates that the presence of α-MnO_2 needles can efficiently improve the cycleability of amorphous MnO_2.

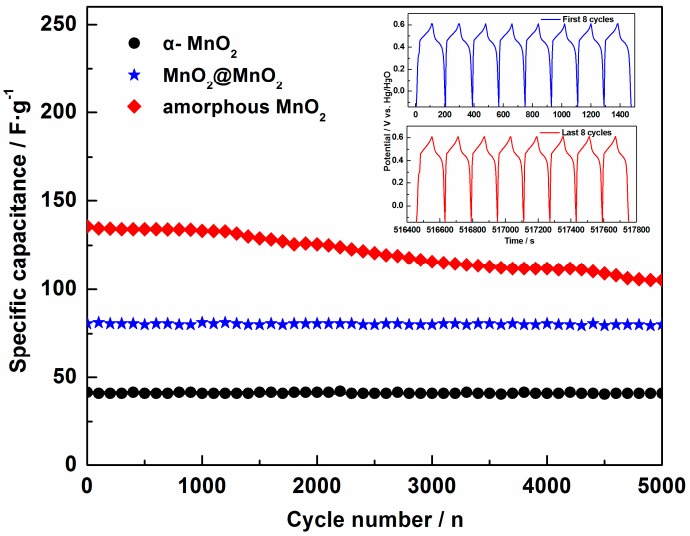

Figure 7. Cyclic stability of the three electrodes in a 1 $mol \cdot L^{-1}$ LiOH electrolyte measured using the galvanostatic charge-discharge technique at a current density of 2 $A \cdot g^{-1}$.

Rate capability testing of MnO_2@MnO_2 was evaluated at current densities ranging from 0.1 $A \cdot g^{-1}$ to 5 $A \cdot g^{-1}$. Figure 8 shows that the specific capacitance decreased as the current density increased, standard finding which is in good agreement with reported literature on MnO_2-based hybrids. From 0.1 $A \cdot g^{-1}$ to 5 $A \cdot g^{-1}$, the specific capacitances of MnO_2@MnO_2 decreased from 150.3 $F \cdot g^{-1}$ to 58.4 $F \cdot g^{-1}$, corresponding to a 38.9% retention of its initial capacitance. The decreasing trend of the capacitance indicates that some parts of the MnO_2@MnO_2 structure are inaccessible for the intercalation

of Li^+ ions at high current density. Compared to some reported MnO_2-based capacitor electrodes [5,30], the rate capability of as-prepared MnO_2@MnO_2 is comparable, which could be ascribed to its unique structure, namely the outer porous structure act as a continuous pathway for the diffusion of electrolyte, which can shorten solid state transport distances for ions into the MnO_2 structure.

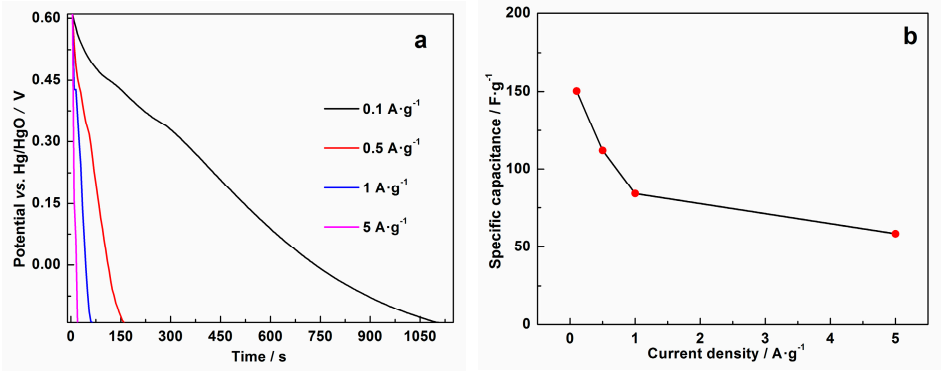

Figure 8. (**a**) Galvanostatic charge-discharge curves of the MnO_2@MnO_2 electrode at different current densities of 0.1, 0.5, 1 and 5 $A{\cdot}g^{-1}$, respectively; and (**b**) variation in specific capacitance with current density obtained based on Figure 8a.

To elucidate the causes behind the difference in capacitance among the three electrodes, EIS experiments were performed. *Nyquist* plots of the three electrodes were generated. Figure 9 displays: (i) semicircles located at the high frequency region which could be related to the charge transfer process at the electrode/electrolyte interface; and (ii) straight lines at the low frequency region possibly ascribed to the ion diffusion process in the bulk of the active mass. It can also be seen in Figure 9 that the semicircles decrease in the sequence of: amorphous MnO_2, MnO_2@MnO_2, and α-MnO_2, suggesting that the charge transfer resistance decreases from amorphous MnO_2 to α-MnO_2. It may be observed that the linear slope of amorphous MnO_2 is larger than that of MnO_2@MnO_2 and α-MnO_2, suggesting that the ion diffusion resistance for amorphous MnO_2 is lower than MnO_2@MnO_2 and α-MnO_2. These results indicate that the charge transfer resistance of amorphous MnO_2 can lead to improved capacitor by mixing with α-MnO_2 needles, but the ion diffusion resistance is increased, which could be attributed to the large different of the porous structure between the amorphous MnO_2 and the α-MnO_2 needles.

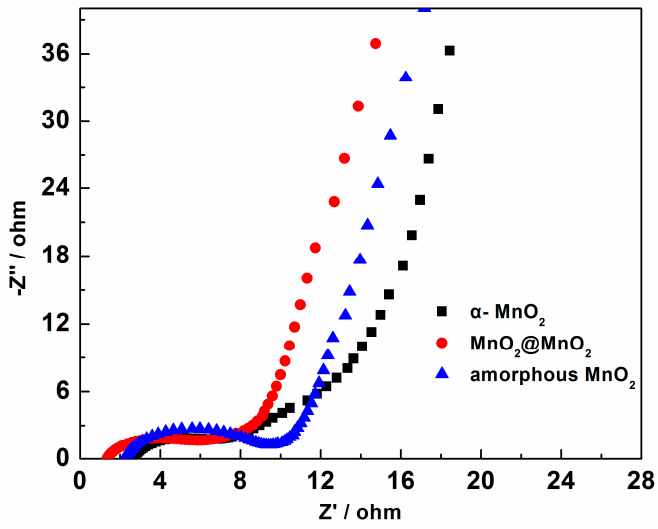

Figure 9. *Nyquist* plots of the electrochemical impedance spectroscopy for the three electrodes.

4. Conclusions

A hierarchical α-MnO_2 nano-needles@amorphous MnO_2 thin nano-sheet core-shell nanostructure was fabricated by a two-step aqueous reaction method. As an electrode for *pseudo*-capacitors, at a current density of 0.1 $A \cdot g^{-1}$, the constructed MnO_2@MnO_2 exhibited a promising specific capacitance of 150.3 $F \cdot g^{-1}$, which consisted of the double-layer charging and Faradaic *pseudo*-capacity. Importantly, nearly 99.3% retention after 5000 cycles at a current density of 2 $A \cdot g^{-1}$ was found. Such intriguing electrochemical properties may be attributed to the hierarchically allomorphs core-shell configuration, in which 1*D* MnO_2 nano-needle core acted as a stable structural backbone and 2*D* amorphous MnO_2 provided a large surface area and more active sites. Thus, the fabricated MnO_2@MnO_2 electrode material with a unique hierarchically allomorphs core-shell architecture are promising candidate material for high-cycleability in Energy Storage Devices.

Acknowledgments: The authors would like to thank the National Natural Science Foundation of China (51362027, 21363022, 21606050 and 51661008) for financially supporting this work.

Author Contributions: R.W. and S.J. conceived and designed the experiments; Q.L. and J.Y. performed the experiments; R.W. and H.W. analyzed the data; H.W., S.J. and B.P. wrote the paper.

Conflicts of Interest: The authors declare no conflict of interest.

References

1. Jiang, R.; Huang, T.; Liu, J.; Zhuang, J.; Yu, A. A novel method to prepare nanostructured manganese dioxide and its electrochemical properties as a supercapacitor electrode. *Electrochim. Acta* **2009**, *54*, 3047–3052. [CrossRef]
2. Wang, J.-G.; Yang, Y.; Huang, Z.-H.; Kang, F. Interfacial synthesis of mesoporous MnO_2/polyaniline hollow spheres and their application in electrochemical capacitors. *J. Power Sources* **2012**, *204*, 236–243. [CrossRef]
3. Li, S.-H.; Liu, Q.-H.; Qi, L.; Lu, L.-H.; Wang, H.-Y. Progress in research on manganese dioxide electrode materials for electrochemical capacitors. *Chin. J. Anal. Chem.* **2012**, *40*, 339–346. [CrossRef]
4. Toupin, M.; Brousse, T.; Be'langer, D. Influence of microstucture on the charge storage properties of chemically synthesized manganese dioxide. *Chem. Mater.* **2002**, *14*, 3946–3952. [CrossRef]
5. Wang, R.; Ma, Y.; Wang, H.; Key, J.; Brett, D.; Ji, S.; Yin, S.; Shen, P.K. A cost effective, highly porous, manganese oxide/carbon supercapacitor material with high rate capability. *J. Mater. Chem. A* **2016**, *4*, 5390–5394. [CrossRef]
6. Minakshi, M.; Mitchell, D.R.G.; Prince, K. Incorporation of TiB_2 additive into MnO_2 cathode and its influence on rechargeability in an aqueous battery system. *Solid State Ion.* **2008**, *179*, 355–361. [CrossRef]
7. Minakshi, M. Examining manganese dioxide electrode in KOH electrolyte using TEM technique. *J. Electroanal. Chem.* **2008**, *616*, 99–106. [CrossRef]
8. Bao, S.-J.; He, B.-L.; Liang, Y.-Y.; Zhou, W.-J.; Li, H.-L. Synthesis and electrochemical characterization of amorphous MnO_2 for electrochemical capacitor. *Mater. Sci. Eng. A* **2005**, *397*, 305–309. [CrossRef]
9. Reddy, R.N.; Reddy, R.G. Synthesis and electrochemical characterization of amorphous MnO_2 electrochemical capacitor electrode material. *J. Power Sources* **2004**, *132*, 315–320. [CrossRef]
10. Xu, C.; Li, B.; Du, H.; Kang, F.; Zeng, Y. Supercapacitive studies on amorphous MnO_2 in mild solutions. *J. Power Sources* **2008**, *184*, 691–694. [CrossRef]
11. Zhan, H.; Zhou, Y.H.; Wang, C.G.; Guo, W.Y.; Peng, Z.H. Improved electrochemical performance of amorphous MnO_2 modified by a novel supermolecular compound. *Mater. Chem. Phys.* **2005**, *90*, 353–360. [CrossRef]
12. Shao, J.; Zhou, X.; Liu, Q.; Zou, R.; Li, W.; Yang, J.; Hu, J. Mechanism analysis of the capacitance contributions and ultralong cycling-stability of the isomorphous MnO_2@MnO_2 core/shell nanostructures for supercapacitors. *J. Mater. Chem. A* **2015**, *3*, 6168–6176. [CrossRef]
13. Ma, Z.; Shao, G.; Fan, Y.; Wang, G.; Song, J.; Shen, D. Construction of hierarchical α-MnO_2 Nanowires@Ultrathin δ-MnO_2 nanosheets core-shell nanostructure with excellent cycling stability for high-power asymmetric supercapacitor electrodes. *ACS Appl. Mater. Interfaces* **2016**, *8*, 9050–9058. [CrossRef] [PubMed]

14. Huang, M.; Zhang, Y.; Li, F.; Zhang, L.; Wen, Z.; Liu, Q. Facile synthesis of hierarchical Co_3O_4@MnO_2 core-shell arrays on Ni foam for asymmetric supercapacitors. *J. Power Sources* **2014**, *252*, 98–106. [CrossRef]
15. Yang, W.; Gao, Z.; Ma, J.; Zhang, X.; Wang, J. Controlled synthesis of Co_3O_4 and Co_3O_4@MnO_2 nanoarchitectures and their electrochemical capacitor application. *J. Alloys Compd.* **2014**, *611*, 171–178. [CrossRef]
16. Wang, K.; Shi, Z.; Wang, Y.; Ye, Z.; Xia, H.; Liu, G.; Qiao, G. Co_3O_4 nanowires@MnO_2 nanolayer or nanoflakes core-shell arrays for high-performance supercapacitors: The influence of morphology on performance. *J. Alloys Compd.* **2015**, *624*, 85–93. [CrossRef]
17. Yan, J.; Khoo, E.; Sumboja, A.; Lee, P.S. Facile coating of manganese oxide on tin oxide nanowires with high-performance capacitive behavior. *ACS Nano* **2010**, *4*, 4247–4255. [CrossRef] [PubMed]
18. Liu, J.; Jiang, J.; Bosman, M.; Fan, H.J. Three-dimensional tubular arrays of MnO_2–NiO nanoflakes with high areal pseudocapacitance. *J. Mater. Chem.* **2012**, *22*, 2419–2426. [CrossRef]
19. Yu, L.; Zhang, G.; Yuan, C.; Lou, X.W.D. Hierarchical $NiCo_2O_4$@MnO_2 core-shell heterostructured nanowire arrays on Ni foam as high-performance supercapacitor electrodes. *Chem. Commun.* **2013**, *49*, 137–139. [CrossRef] [PubMed]
20. Ma, Y.; Wang, R.; Wang, H.; Key, J.; Ji, S. Control of MnO_2 nanocrystal shape from tremella to nanobelt for ehancement of the oxygen reduction reaction activity. *J. Power Sources* **2015**, *280*, 526–532. [CrossRef]
21. Brunauer, S.; Demine, L.S.; Deming, W.E.; Teller, E. On a theory of the van der Waals adsorption of gases. *J. Am. Chem. Soc.* **1940**, *62*, 1723–1732. [CrossRef]
22. Zhou, T.; Wang, H.; Ji, S.; Linkov, V.; Wang, R. Soybean-derived mesoporous carbon as an effective catalyst support for electrooxidation of methanol. *J. Power Sources* **2014**, *248*, 427–433. [CrossRef]
23. Qu, Q.; Zhang, P.; Wang, B.; Chen, Y.; Tian, S.; Wu, Y.; Holze, R. Electrochemical performance of MnO_2 nanorods in neutral aqueous electrolytes as a cathode for asymmetric supercapacitors. *J. Phys. Chem. C* **2009**, *113*, 14020–14027. [CrossRef]
24. Sodtipinta, J.; Pon-On, W.; Veerasai, W.; Smith, S.M.; Pakawatpanurut, P. Chelating agent- and surfactant-assisted synthesis of manganese oxide/carbon nanotube composite for electrochemical capacitors. *Mater. Res. Bull.* **2013**, *48*, 1204–1212. [CrossRef]
25. Pang, M.; Long, G.; Jiang, S.; Ji, Y.; Han, W.; Wang, B.; Liu, X.; Xi, Y. Rapid synthesis of graphene/amorphous α-MnO_2 composite with enhanced electrochemical performance for electrochemical capacitor. *Mater. Sci. Eng. B* **2015**, *194*, 41–47. [CrossRef]
26. Zhao, Y.; Meng, Y.; Jiang, P. Carbon@MnO_2 core-shell nanospheres for flexible high-performance supercapacitor electrode materials. *J. Power Sources* **2014**, *259*, 219–226. [CrossRef]
27. Han, D.; Jing, X.; Xu, P.; Ding, Y.; Liu, J. Facile synthesis of hierarchical hollow ε-MnO_2 spheres and their application in supercapacitor electrodes. *J. Solid State Chem.* **2014**, *218*, 178–183. [CrossRef]
28. Lee, T.T.; Hong, J.R.; Lin, W.C.; Hu, C.C.; Wu, P.W.; Li, Y.Y. Synthesis of petal-like carbon Nanocapsule@MnO_2 core-shell particles and their application in supercapacitors. *J. Electrochem. Soc.* **2014**, *161*, H598–H605. [CrossRef]
29. Min, S.; Zhao, C.; Zhang, Z.; Wang, K.; Chen, G.; Qiana, X.; Guo, Z. Hydrothermal growth of MnO_2/RGO/$Ni(OH)_2$ on nickel foam with superior supercapacitor performance. *RSC Adv.* **2015**, *5*, 62571–62576. [CrossRef]
30. Ren, Q.; Wang, R.; Wang, H.; Key, J.; Brett, D.J.L.; Ji, S.; Yin, S.; Shen, P.K. Ranunculus flower-like $Ni(OH)_2$@Mn_2O_3 as a high specific capacitance cathode material for alkaline supercapacitors. *J. Mater. Chem. A* **2016**, *4*, 7591–7595. [CrossRef]